Materials & Design 259 (2025) 114920

Contents lists available at ScienceDirect

Materials & Design

journal homepage: www.elsevier.com/locate/matdes

Nanotopography-driven changes in focal adhesion morphology of human dermal fibroblast cells on inkjet-printed hierarchically structured hemitoroids

Emil Rosqvist [a,*], Anna Fogde [a], Elnaz Fazeli [b,c], Irina Belaya [d], Erik Niemelä [e], Anni Määttänen [a], Arun P. Venu [e], Pasi Kankaanpää [d], John E. Eriksson [d,e], Jouko Peltonen [a]

[a] Laboratory of Molecular Science and Engineering, Åbo Akademi University, Henriksgatan 2, Åbo FI-20500, Finland
[b] Laboratory of Biophysics, Faculty of Medicine, University of Turku, Turku, Finland
[c] Biomedicum Imaging Unit, Faculty of Medicine and HiLIFE, University of Helsinki, Finland
[d] Turku BioImaging, Åbo Akademi University and University of Turku, Artillerigatan 6, Åbo FI-20520, Finland
[e] Laboratory of Cell Biology, Åbo Akademi University, Artillerigatan 6, Åbo FI-20520, Finland

ARTICLE INFO

Keywords:
Latex
Roughness
HDF
Polymer particle dispersion
Focal adhesion
Morphology
STED
Stimulated depletion emission microscopy

ABSTRACT

Two-component polymer particle dispersions can be used to make nanostructured coatings with diverse applications. In this study, blends of polystyrene and acrylonitrile butadiene styrene latex dispersions were formulated for inkjet printing. When printed onto glass coverslips with a 50 μm drop spacing (DS) the result was ultrathin, nanostructured coatings. Increasing the DS to 100 μm produced arrays of nanostructured hemitoroids approximately 30–60 μm in diameter. By adjusting the blend ratio, the nanotopography of the hemitoroids could be tuned (e.g. S_q 6–32 nm).

These hemitoroid arrays, which exhibited different nanotopographies, were used for studying the influence of nanotopography on the morphology of focal adhesions (FAs) of human dermal fibroblast cells. Statistically significant differences in FA shape (e.g. roundness and aspect ratio) and size (area and perimeter length) were observed for different latex blends — even when the difference in RMS roughness (S_q) was only 3.9 nm. Strong correlations were observed between FA morphology and surface roughness in terms of S_a, S_q, S_{dr}, S_{pk}, and S_k ($R^2 \geq 0.9$ and Pearson's $r \geq |0.95|$), indicating that the response in FA morphology was mainly driven by nanoscale height variations and fine texture of these surfaces. These findings hence highlight the role of nanotopography in modulating substrate-cell signal transduction.

1. Introduction

During physiological and cellular processes, cells interact with the surrounding cells, the surrounding materials, and the extracellular matrix (ECM), through response-driving cues [1]. This interplay is the central process around which biomaterials function, where mechanical signals, from for instance physical forces or geometric features, are converted into biochemical signals by cells and vice versa, in a process called mechanostransduction [1,2]. However, the complexity of the ECM presents challenges in understanding cell-surface responses in detail.

To add to the challenge, cellular responses are also modulated by various materials properties such as surface topography across multiple length scales, surface chemistry, surface charge, and material stiffness. These properties can drive essential cellular behaviours, such as cell adhesion, migration, and proliferation [1]. Biomaterials engineered to regulate these essential cellular processes, which are active in e.g. regenerative processes, can make medical devices more compatible with biological systems and reduce complications [3]. As an example, the response of antigen-presenting cells, which are crucial e.g. in implant healing, can be controlled by modifying topography and surface chemistry [4]. Such insights underscore the importance of designing biomaterials that actively engage with cellular mechanisms to promote favourable biological outcomes.

Cell-ECM adhesion is mediated through the formation of supramolecular protein complexes (focal adhesions), which are typically smaller

* Corresponding author.
E-mail address: emil.rosqvist@abo.fi (E. Rosqvist).

https://doi.org/10.1016/j.matdes.2025.114920
Received 9 April 2025; Received in revised form 24 September 2025; Accepted 10 October 2025
Available online 12 October 2025

than 200 nm. These are the primary mediators of the mechanotransduction [2]. These complexes consist of an integrin signalling layer, a force transduction layer, and an actin regulatory layer, enabling cells to sense biochemical, geometrical, and mechanical cues from the environment [5]. Through these interactions, cells sense the properties of their surroundings, and respond to these directly or via signal transduction pathways that regulate cellular behaviour [1].

Integrin clustering activates focal adhesion kinase (FAK) through autophosphorylation, which in turn reactivates integrins to increase binding strength. Activated FAK promotes the activity of Rac1 and Rap, facilitating actin polymerisation, dynamic cell adhesion (e.g. through protrusion formation) and adhesion maturation [1]. With this central role in mind, analysing focal adhesion dynamics offers a powerful tool to evaluate the functional activity of biomaterial surfaces [6].

While both 2D and 3D systems share many features, they differ in aspects such as FA composition and cell morphology. Nevertheless, 2D systems remain a practical and widely accepted model for studying cell-material interactions of biointerface materials for implants and similar devices. [1]. Therefore, experimental protocols should be carefully selected to ensure relevance to the intended application.

Topography-driven changes in the focal adhesion formation of cells have been studied in various contexts. For example, micrometre-scale roughness of stainless steel and titanium surfaces has been shown to influence the number, size and dynamics of focal adhesion [6]. Heights of nano-island topographies in the range of 10–20 nm have been observed to promote adhesion and spreading of endothelial cells as well as fibroblasts (using a blends of polystyrene (PS) and poly(4-bromostyrene)). Similar observations have also been done for mesenchymal stem cells (using titanium-based materials) [1–9]. In contrast, features exceeding a height of approx. 100 nm have been observed to inhibit human fetal osteoblastic (hFOB) cell spreading using poly(L-lactic acid (PLLA) and PS surfaces). On surfaces with lower feature heights a lower FAK expression was observed in hFOB cells [10].

Compared to flat surfaces, both randomly oriented and regularly oriented surface structures have been observed to yield an enhanced cell adhesion and growth, possibly through FAK activation. However, many of these studies provide only limited characterization of surface topography, often restricted to single images or basic roughness metrics. FAK has also been indicated to increase Rho activity, stress fibre formation, and adhesion modulation [1–11].

In addition to topography, ligand spacing has been shown to influence focal adhesion formation [5]. Studies using nanopatterned surfaces have revealed that ligand spacings above 140 nm inhibit focal contact formation, while spacings beyond 400 nm prevented cell spreading. Ligand spacings above 90 nm decreased adhesion forces compared to 50 nm spacings. The general conclusion was that the optimal ligand spacing was around 60 nm, corresponding to 4–5 integrins [5]. A theoretical model has estimated the critical spacing of receptor-ligand spacing to be approx. 39–89 nm wide [12]. De Beer et al. further refined the understanding by analysing ligand spacing from reaction kinetic and force distribution perspective, and concluded the ligand periodicity to be stable below 76 nm, unstable between 76 nm and 93 nm, and "forbidden" above 93 nm [13].

Surface energy also plays a role in modulating FA behaviour and has been observed to influence the formation of focal adhesions. For instance, a higher surface energy of titanium surfaces have been observed to improve early adhesion of osteoblast cells [14]. On gelatin-methacryloyl hydrogels with varying roughness (R_q = 54–1200 nm) and stiffness (3.8 kPa – 31.3 kPa), human mesenchymal stem cells showed a stiffness-dependent response to roughness [15]. These studies collectively highlight how even subtle variations in surface geometry can significantly influence focal adhesion formation.

Polymer particle dispersions, commonly referred to as latex, represent a highly versatile class of materials that can be engineered to exhibit a wide range of properties and readily processed into coatings and films. These colloidal systems consist of polymer particles dispersed in a liquid medium and have long been used in industries such as paper converting, paints, coatings, textiles and leather. More recently, their utility has been expanded into biomedical and biotechnological applications to the possibility of functionalising the dispersed particles with biomolecules, e.g. by conjugation with antigens [16,17].

Latex dispersions can be deposited onto surfaces using a diverse range of techniques, including heat transfer printing [18], bar coating [19], inkjet printing [20], screen-printing [21] flexographic printing [22], and reverse gravure coating [23] allowing for their use in large scale applications. The surface character of the resulting films (for instance surface energy and wettability, surface roughness, topography, as well as viscoelastic properties) are determined by the chosen polymer or polymer blend used [24,25]. This high degree of tunability makes latex-based materials well-suited for biological interfaces and cell-surface interaction studies.

In previous work, we have demonstrated the modulating effect of the roughness of nanostructured PS:ABS (acrylonitrile butadiene styrene) latex coatings on the growth of HDF cells [26] and HeLa cells [27]. The coatings have also been observed to influence the growth and poly-β(1–6)-N-acetylglucosamine (PNAG) expression of *Staphylococcus aureus* biofilms, as well as modulate the abundance of virulence associated surface proteins, through the surface characteristics [25]. The processability of the films has also been utilised on a large scale for reliable, surface tunable cell culture platforms [28,29], as substrates for surface-enhanced Raman spectroscopy (SERS) [23], and as supports for semi-transparent electrodes [30].

In this study, the intent was to focus on the printability of the PS:ABS latex blends, and to utilise the obtained nanostructured features to investigate material-cell interaction at the level of focal adhesions in human dermal fibroblasts. These studies were intended shed more light on the responses of HDF cells to nanometer level variations in the topography of latex coatings that were observed in [27]. Further, human dermal fibroblasts are active in wound healing and understanding their responses to implant and prosthodontic surfaces are critical to understand in depth. The optical transparency of the latex films enabled direct observation of how nanoscale surface features influence cell proliferation by modulating adhesion. A key research question was whether topographical differences on the scale of just a few nanometres could be enough to drive differences in the focal adhesion morphology. Unlike previous studies, we used several different roughness parameters to relate the observed responses to a range of different topographical properties, as has been recommended in literature [31–34].

2. Materials and methods

2.1. Substrates

Borosilicate cover glasses (Ø = 13 mm) and microscope slides (76 × 26 mm, Thermo Scientific) were used as support substrates. Prior to printing, the glasses were cleaned by rinsing, first with water and then with ethanol, followed by a plasma cleaning treatment for 2 min (Medium setting, PDC-326, Harrick).

2.2. Printing of the latex films

The ink was prepared by diluting an aqueous latex blend (solids content approx. 50 %) with a solvent mixture H_2O:EG (ethylene glycol): IPA(isopropanol alcohol) at a ratio of 70:20:10. The final ink formulation consisted of a 1:12 vol ratio of latex dispersion to solvent mixture.

The latex blend consisted of two different latex dispersions: polystyrene (PS) and carboxylated acrylonitrile butadiene styrene (ABS). The PS dispersion (HPY83, Styron Europe GmbH, CH) consisted of particles with the average particle size of 130 nm and glass transition temperature (T_g) of 105 °C (information provided by the supplier). The ABS copolymer had a T_g of 8–10 °C and an average particle size of 140 nm (HPC26, DOW Europe GmbH, CH, information provided by

supplier). In this study, blend compositions are referred to by their PS content, for example, a 70:30 PS:ABS ratio is named 70 % PS. The selected blends, 0 % PS, 30 %, 50 %, 60 % PS, and 70 % PS, were chosen to show a wide range of topographies as well to cover as different HDF cell yields as possible, based on the observations in [26].

Inkjet printing was performed under ambient conditions (T = 23 ± 2 °C, RH = 35 ± 8 %,) using a piezoelectric Dimatix™ Materials Printer (DMP-2800, FUJIFILM Dimatix, Inc. Santa Clara, USA). Printing was performed by depositing 10 pL droplets from a replaceable cartridge (DMC-11610) using a firing voltage of approx. 22 V and a custom waveform optimized for droplet formation. After printing, the substrates were washed with MilliQ water and ethanol.

Sintering of the printed latex films was carried out for 40 s using a shortwave IR drier (IRT systems, Hedson Technologies AB, Sweden) consisting of three 30 cm long 2 kW strip light bulbs. The distance between the sample and the lamp during drying was approximately 20 cm.

2.3. UV–vis spectroscopy

Transmission UV–vis spectroscopy measurements were carried out using a Lambda 900 spectrometer (PerkinElmer, USA) with a PELA-1020 integrating sphere setup.

2.4. Atomic force microscopy

Topographical characterization of the latex coatings was conducted with a NanoScope V MultiMode 8 atomic force microscope (AFM, Multimode™, Bruker). Image analysis was done using MountainSPIP software (v. 9.3.10663, Digital Surf, Besançon, France). The used tips, HQ:NSC14/Al BS (k = 5N/m), were manufactured by μMasch (Bulgaria), and had a nominal tip radius of < 8 nm reported by the manufacturer.

Adequate description of surfaces requires the use of several different roughness parameters beyond the common S_a and/or S_q parameters [31–34]. In this study, we used a range of parameters to describe aspects of the surface topography, including the amplitude, the spacing between features and height distributions, but also the height of peaks and depth of the valley regions.

These were; The amplitude parameters S_a and S_q, which describe the average height variations from the mean level as the arithmetic mean value (S_a) respectively the root mean square value (S_q), of each measurement point of the surface. These correspond to the R_a and R_q parameters often found in especially older literature, with the difference that S-parameters are determined from the imaged area rather than line-by-line, as R-parameters are calculated. Of these parameters, S_a is common in standards while S_q is considered more statistically robust [35,36]. A measure of the lateral roughness is the S_{al}, the autocorrelation length, or the distance over which the autocorrelation drops to 10 % of its original value. The effective surface area, S_{dr}, describes the increased surface area due to roughness in comparison to the projected, that is a completely flat, image area. The skewness, S_{sk}, and kurtosis, S_{ku}, parameters describe the distribution of heights; The S_{sk} describes the asymmetry of the distribution around the mean value. A positive (>0) S_{sk} of a height distribution indicates that peaks dominate the distribution, while a negative S_{sk} indicates a surface being dominated by valleys. A symmetric, Gaussian distribution has a S_{ku} of 3. Higher and lower values indicate broader respectively narrower distributions. A measure of the fine texture is given by S_{ds}. This parameter gives the number of asperities, local peaks surrounded by lower points per surface area. The parameters S_{pk} (the reduced peak height), S_k (the core roughness), and S_{vk} (the reduced valley depth), are obtained from the material ratio curve. This is a plot of the sum of the ratio material intercept through a bearing plane (a plane parallel with the mean plane), with the material ratio determined at each height as it passes through a measured surface plot. S_k is the depth of the core roughness profile. This is determined by fitting a least mean squares line (LMS) to the material ratio curve, so the LMS line gets the lowest decline. The depth is calculated from the level of the points of extrapolation when the LMS line is extrapolated to 0 % and 100 % material ratio. The parameters S_{pk} and S_{vk}, meanwhile, are the average height of the highest peaks above the core roughness profile, respectively the average depth of the deepest valleys below the core roughness profile [32].

PeakForce NanoScope V MultiMode 8 atomic force microscope (AFM, Multimode™, Bruker) mode was used to analyse the stiffness (DMT modulus) of 50 % PS, 60 % PS, and 70 % PS surfaces. Analysis was done from 5 μm x 5 μm images with a digital resolution of 512 px x 512 px, using MountainsSPIP software (v. 9.3.10663, DigitalSurf, Besançon, France). Cantilevers of type NSC15 (with k≈40 N/m) were used. The mode value was from each of 6 images of each sample type (2 images of 3 replicates) was averaged to obtain the reported values. The standard deviation was used as error.

2.5. Cell studies

For cytocompatibility tests, human dermal fibroblasts (HDF) cells were seeded at a density of 10 k cells on the cover slip substrates and incubated for 24 h at 37 °C and 5 % CO_2 in DMEM media with high glucose (# D5671, Sigma-Aldrich, USA) supplemented with 10 % fetal calf serum (Biowest), 2 mM L-glutamine, 100 U ml^{-1} penicillin, 100 μg ml^{-1}/ streptomycin.

2.6. STED imaging

For 2D STED imaging (stimulated emission depletion microscopy), cell seeding was done following the same protocols as the cytocompatibility tests. After 24 h cells were fixed using 4 % PFA for 10 min. Cells were washed thrice with PBS and then permeabilized with 0.2 % Triton X-100 in PBS for 15 min at RT, washed thrice in PBS, blocked with 5 % Goat serum in PBS for 1 h in RT. Then the coverslips were incubated on top of 100 μl drops of primary Anti-Paxillin rabbit antibody (E228) by Abcam or Anti-FAK rabbit (phospho Y397) antibody [EP2160Y] by Abcam in 5 % Goat serum in PBS for 1 h at RT, dip washed ten times in PBS, incubated on 100 μl drops of secondary Abberior Star 635P anti-rabbit antibody for 1 h at RT, dip washed the coverslips using forceps ten times in PBS, rinsed thrice in MilliQ water and mounted with Mowiol mounting media. Samples were imaged with Abberior STED microscope equipped with a Photo Multiplier Tube using 100x/1.4NA Olympus UPLSAPO oil immersion objective. A pulsed 775 nm laser was used for depletion. The imaging was done with optimised parameters that were kept constant throughout the imaging, to ensure comparability of results and quantitative analyses.

2.7. Light microscopy for observing cell proliferation on large surface area

Before microscopy HDF cells were seeded at a density of 100 k cells on 22 x 22 mm^2 glass coverslips or on inkjet coated 22 x 22 mm^2 glass coverslips that were placed in 6-well plates for cell culturing. Samples were sterilised using 70 % ethanol and air dried in RT before cell plating. Cell growth was monitored in complete DMEM cell medium using ZEISS Axiovert 5 light microscope over a period of 6 days, taking images daily.

2.8. Crystal violet staining for quantifying cell growth

For the crystal violet cell growth quantification, HDF were seeded at a density of 100 k cells on sterilized 13 mm glass coverslips or sterilized inkjet coated 13 mm glass coverslips that had been placed in 24-well plates for seeding. After 24 h of incubation the HDF cells were washed with phosphate buffered saline (PBS), and the nuclei were stained using 0.2 % crystal violet dye (CV) in a 2 % ethanol solution. Excess dye was rinsed off with repeated MilliQ water washing cycles, and then air-dried in RT. After drying, the CV was re-solubilized in 2 % sodium dodecyl sulphate (SDS) and the absorbance of each well was determined at 570

nm using a HIDEX micro plate reader (Hidex, Finland). The absorbance of each sample at the end point was normalized to the mean value of the glass coverslip samples measured in parallel to give the cell growth. This end point measurement gives the cytocompatibility estimate of HDF cells grown on said materials.

2.9. Image analysis

For analysis of focal adhesion parameters of HDF cells within three regions of interest (glass, the hemitoroid, i.e. the doughnut-shape, and the centre of the hemitoroid, i.e., the area limited by the inner diameter of the hemitoroid) of hemitoroids of three different vol.:vol. PS:ABS blend-ratios of latex (50 %, 60 %, and 70 % PS) ImageJ software, version 1.54f was used [37]. Focal adhesions of HDF cells cultured on an uncoated glass surface were analysed as a control. First, to smoothen the images and remove noise the "Gaussian blur" (sigma radius s = 3) filter was applied. To detect focal adhesions, manual intensity thresholding was used to convert each grayscale image to a binary image. The thresholding value was set for each image using the same protocol based on the histogram and visual inspection. With the "analyse particle" command, structures below 1 μm^2 were excluded from the binary images to limit the analysis to focal adhesions, and then the parameters of focal adhesions were measured: area (μm^2), perimeter (μm), the major and the minor axis of the best-fit ellipse, circularity ($\frac{4\times\pi\times area}{perimeter^2}$), aspect ratio (AR, $\frac{majoraxis}{minoraxis}$), solidity ($\frac{area}{convexarea}$), where the convex area here is the area of the smallest convex polygon that encloses a selected focal adhesion), and roundness ($\frac{4\times area}{\pi\times majoraxis^2}$). For circularity and roundness, a value of 1.0 indicates a perfect circle while a value of 0.0 indicates an increasingly elongated shape. Statistical analysis of the data was performed by using GraphPad Prism version 8.4.2 for Windows (GraphPad Software, Boston, Massachusetts USA, www.graphpad.com). The data was tested for normal distribution and statistical outliers were detected using Grubb's test. Non-parametric Mann-Whitney *t*-test was used to determine the statistical significance between mean values. The values are expressed as means ± SEM and statistical significance was considered at $p < 0.05$.

Analysed numbers (n) were: Control – 148; 50 % PS – 11 for area outside doughnut and 52 for hemitoroid area; 60 % PS – 25 for area outside doughnut and 49 for hemitoroid area; 70 % PS – 20 for area outside doughnut and 108 for hemitoroid area.

3. Results

3.1. Inkjet printing

To evaluate printability, ink formulations based on a 50 % PS latex blend were first inkjet-printed onto glass coverslips. An ink formulation based on a solvent mixture of H_2O:EG:IPA (70:20:10) yielded good printability and resulted in homogeneous coating. A drop spacing (DS) in the range 50 μm to 80 μm between the printed drops, after a plasma cleaning, which increased the wettability of the substrate, resulted in an optimal print quality. These films showed a high optical transparency of > 98 %, whereas drop-cast films showed transparency in the range of 90–95 % in most of the visible regions.

Hierarchically structured surfaces featuring organized arrays of hemitoroidal features were then fabricated via inkjet printing. This was achieved by increasing the DS during printing to > 100 μm and reducing the plasma treatment to limit the spreading of the printed droplets. Different spacings between hemitoroids were obtained by adjusting the DS.

These structures could be printed directly onto glass substrates or onto surfaces pre-coated with a continuous latex film (see Fig. 1B). The hemitoroids had diameters of approximately 60 μm when printed onto pre-coated latex surface. When printed onto borosilicate glass, the 'hemitoroids' were roughly 40 μm wide, similar in size as cells, with an inner diameter of 15–20 μm and a height of 400–800 nm. They typically had a circular outline.

Using this approach, entire surfaces could be uniformly covered with hemitoroidal features (Fig. 1B). When printed directly onto a supporting material, such as glass, a comparison of cellular responses to said nanostructured hemitoroids and the unstructured support material could be investigated in the same *in vitro* culture. This allowed for assessing how individual cells respond to different surface topographies while limiting the influence of phenotype changes caused by attachment to different materials.

3.2. Topography and stiffness characterisation

The topography of the hemitoroidal structures and the inkjet-printed film was analysed with AFM (Fig. 2 and Fig. 3). Using an ink with only ABS (0 % PS) resulted in a very smooth surface, but as PS was added to the ink, the amount of protruding PS asperities on the surface increased with PS content, thus increasing the height variations and roughness. At approximately equal proportions of PS and ABS, most of the surface was covered by the PS particles. The centre of the hemitoroid, exhibited a markedly different topography compared to the toroidal ring, and with a mesh-like structure of latex (Fig. 3B). Between blends this mesh-like geometry did not differ noticeably in overall structure.

3.3. Similarly, the inkjet-printed film also showed a surface mostly covered by PS with intermittent valleys

The inkjetted films had a quite low roughness despite of their nanostructure (Fig. 4, Fig. 5, and Supplementary Table 1). The amplitude roughness parameters, S_a and S_q, were approx. 5 nm respectively 6.5 nm, with a S_{dr} of only 1.4 %. This roughness was also valley-dominated, with S_{sk} approx. −0.9. The surface of the ring of the 100

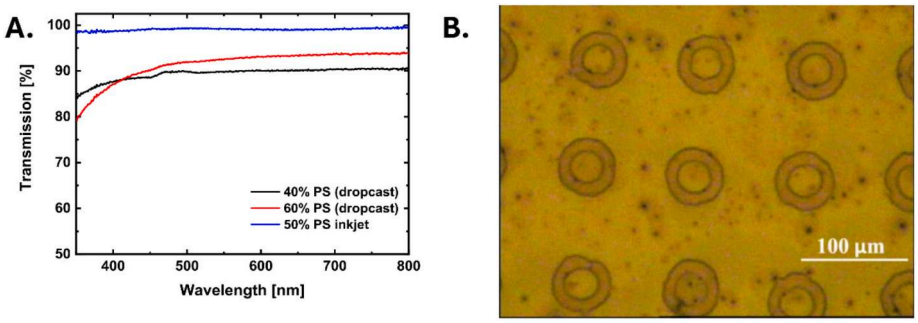

Fig. 1. A. Transmission spectra of drop cast latex onto cover slips (40:60, black and 60:40, red) compared to inkjet-printed 50% PS coatings (blue). B. Optical micrograph of latex hemitoroids printed on top of latex film (First layer DS50, second layer DS100). (For interpretation of the references to colour in this figure legend, the reader is referred to the web version of this article.)

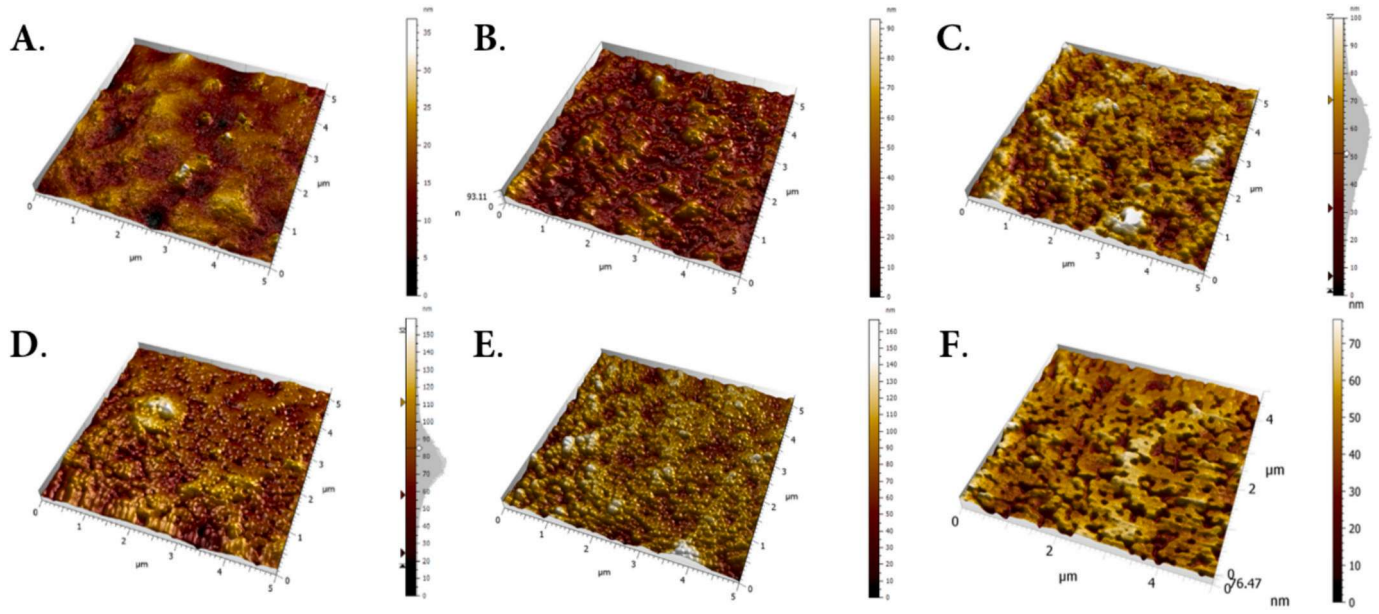

Fig. 2. Representative images of the nanostructure of hemitoroid rings with different latex blends deposited by inkjet printing onto glass: A) 0% PS hemitoroid, B) 30% PS hemitoroid, C) 50% PS hemitoroid, D) 60% PS hemitoroid, E) 70% PS hemitoroid, and F) 50% PS film.

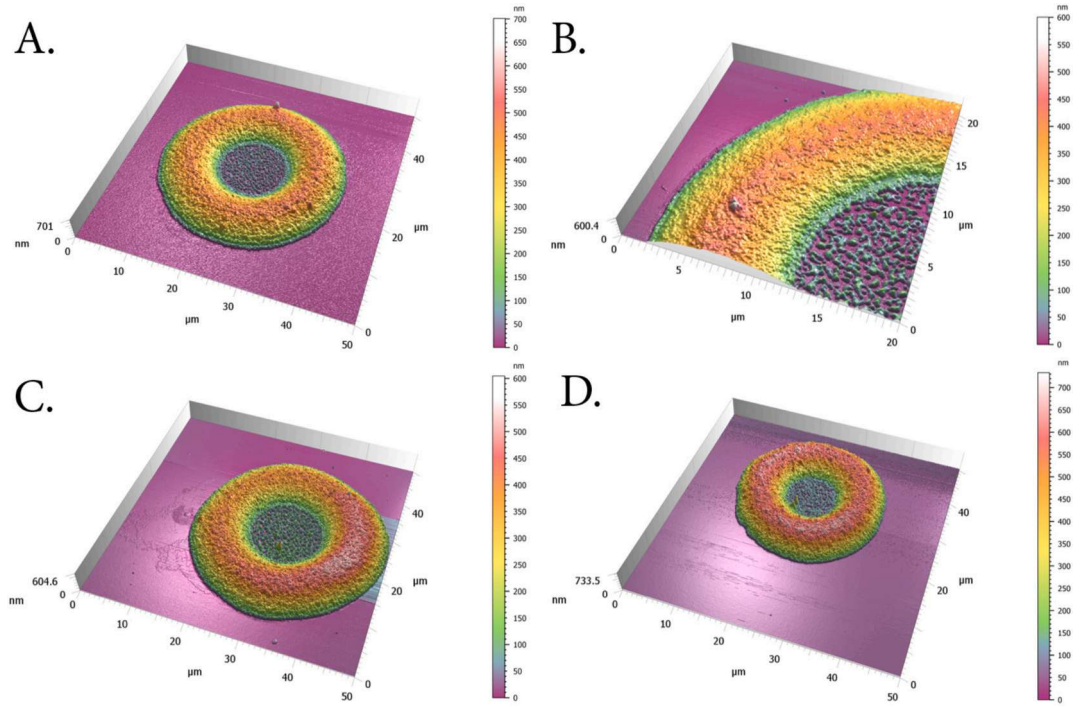

Fig. 3. Representative AFM images of hemitoroids with varying PS content deposited onto glass: A) 30 % PS hemitoroid (50 µm x 50 µm), B) detail of 30 % PS hemitoroid ring showing the fine structure of the centre area (20 µm x 20 µm), C) 50 % PS hemitoroid (50 µm x 50 µm), and D) 70 % PS hemitoroid (50 µm x 50 µm).

% ABS hemitoroid was smooth, with an amplitude roughness similar to the 50 % PS film (S_a approx. 4.5 nm, S_q approx. 6.4 nm), and a very low S_{dr} (0.18 %). The S_a, S_q, and S_{dr} increased progressively for the samples, except between 50 % and 60 % PS. The difference in roughness between these two samples was in their kurtosis (S_{ku}) and skewness (S_{sk}), with the 60 % PS being more peaked (higher S_{ku}) than the 50 % PS. The 60 % PS also had a peak-dominated structure (S_{sk} approx. 0.31), while the 50 % PS was neither peak nor valley dominated (S_{sk} approx. 0). The hemitoroid surface with the highest S_q was the 70 % PS (S_q approx. 19 nm).

The central region of the hemitoroids exhibited a relatively high roughness with a S_a and S_q of approx. 28 nm and 32 nm, respectively. This region also a high effective surface area, S_{dr} approx. 14 %, and was neither clearly peak nor valley dominated with a kurtosis of (1.9).

The stiffness (DMT modulus) of the samples was also analysed with PeakForce Tapping™. The stiffness was determined to be 1.48 ± 0.64 GPa for 50 % PS, 1.90 ± 1.02 GPa for 60 % PS, respectively 2.00 ± 1.31 GPa for 70 % PS (Supplementary Fig. 35).

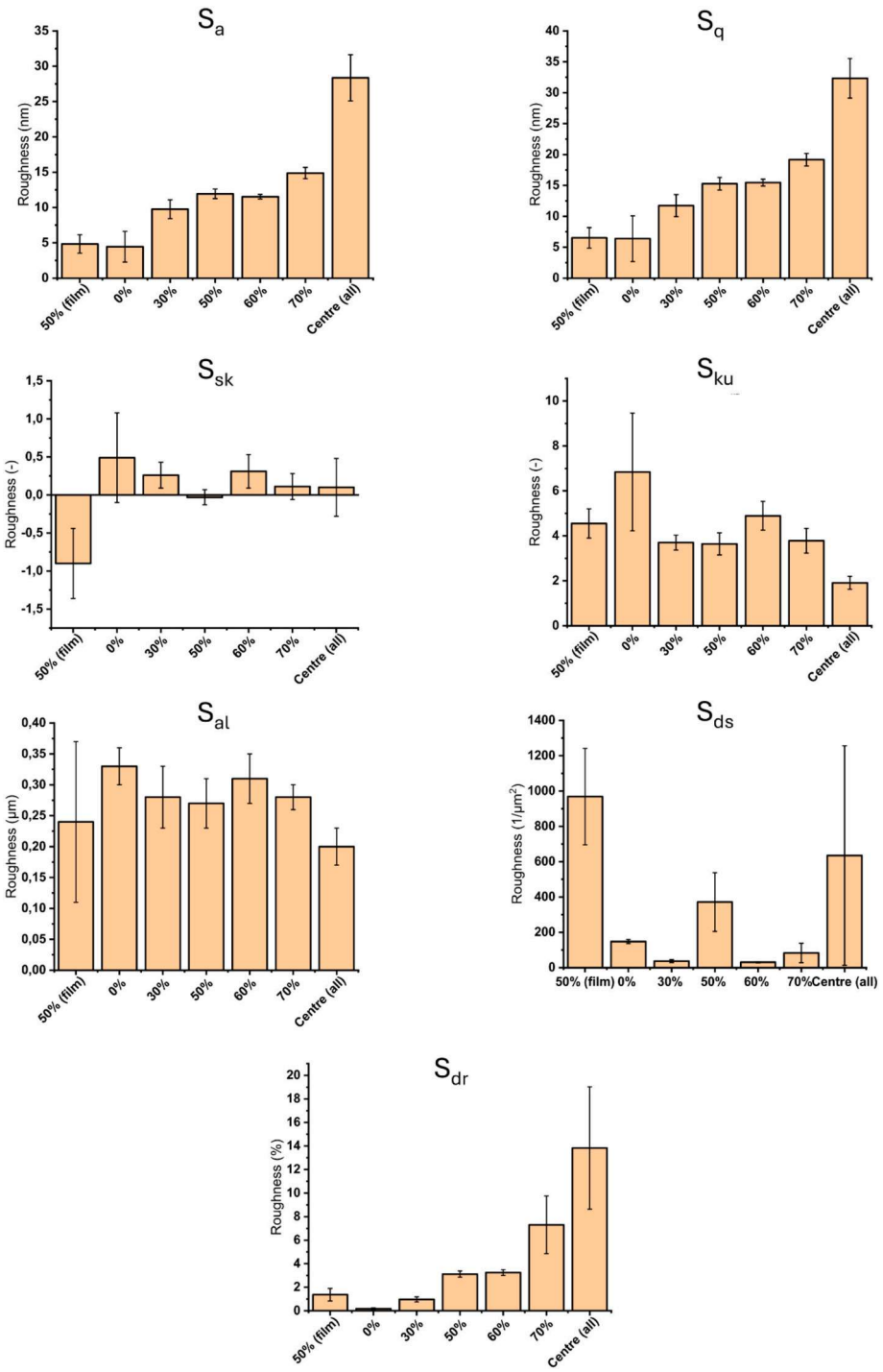

Fig. 4. Measured roughness described with the parameters S_a, S_q, S_{sk}, S_{ku}, S_{al}, S_{ds}, and S_{dr} for the different surfaces: 50 % PS printed as a film (50 % film), as well as the hemitoroid surface of blends with 0 %, 30 %, 50 %, 60 %, and 70 %, as well as the average centre structure. The shown error is the standard deviation (n = 3).

3.4. Cytocompatibility of the surfaces

Cytocompatibility of the 50 % PS DS50 surfaces was assessed with a viability assay (Fig. 6A). These results were compared to two reference surfaces: standard well plates (Cellstar) and uncoated borosilicate glass coverslips. It was observed that the cell growth on the inkjetted latex surface was as high as on the two reference surfaces. The substrates thus showed a good apparent cytocompatibility.

The growth of HDF cells on all three substrates was similar in terms of morphology and health of the cells in comparison to cells grown on glass and plastic substrate cell culture dish (Cellstar) as seen in Fig. 6, Supplementary Fig. 9 to Supplementary Fig. 11. There was no apparent apoptosis or senescence noticed.

3.5. Focal adhesion imaging

The printed nanostructured hemitoroidal array surfaces were then deployed to compare the morphology of the focal adhesions between HDF cells attached to surfaces with different nanotopography and borosilicate glass areas based on STED images of cells attached to both the latex hemitoroids and glass, as well as cells attached to borosilicate glass as control (Fig. 7). The analysis focused on several morphological

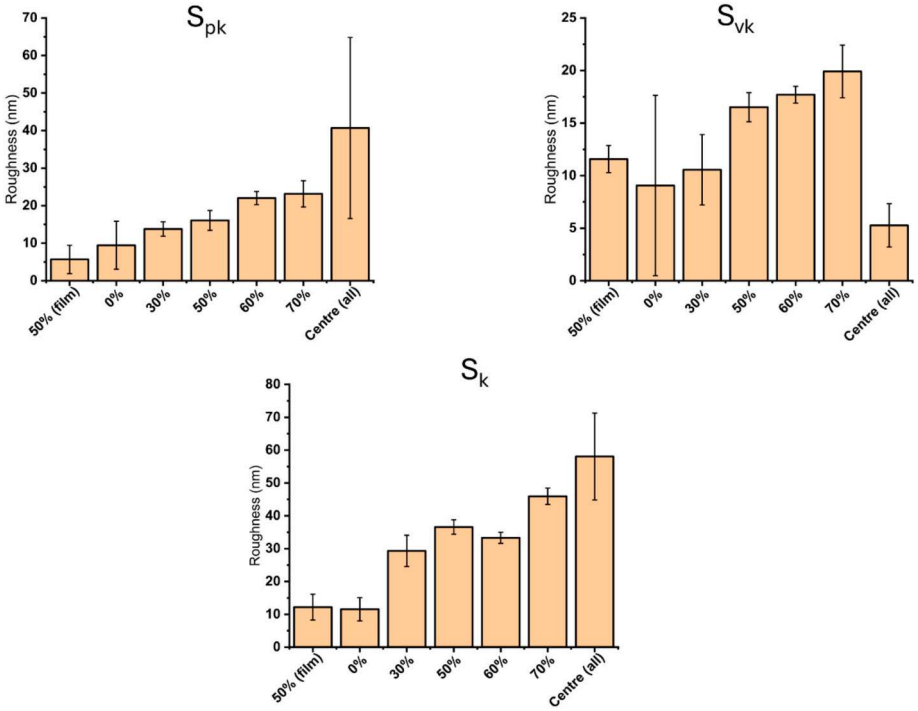

Fig. 5. Measured roughness described with the parameters S_{pk}, S_{vk}, and S_k for the different surfaces: 50 % PS printed as a film (50 % film), as well as the hemitoroid surface of blends with 0 %, 30 %, 50 %, 60 %, and 70 %, as well as the average centre structure. The shown error is the standard deviation (n = 3).

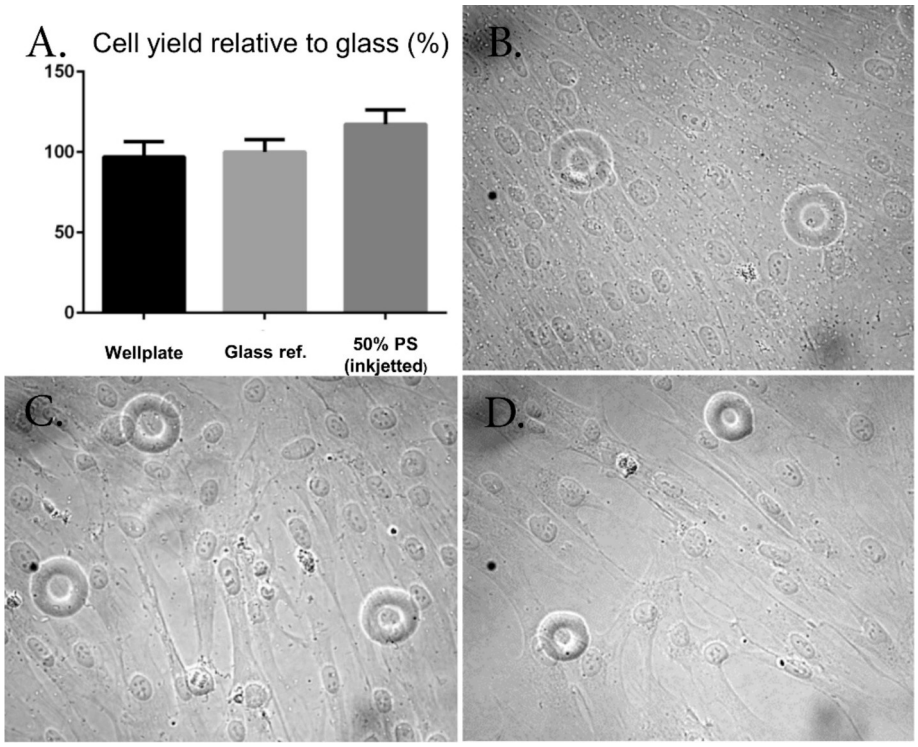

Fig. 6. A. Results from cytocompatibility studies showing relative HDF cell numbers at the endpoint (72 h) on well plate (reference), uncoated glass, and an inkjet-printed DS50 layer of 50 % PS. Representative microscopy images of HDF cells grown on the hemitoroids made by inkjet deposition of different latex blends onto glass: B. 0 % PS, C. 30 % PS, and D. 50 % PS.

parameters of the focal adhesions.

The analysed morphological parameters were:

i) Their size, in terms of area and their perimeter length (Fig. 8, Supplementary Fig. 18, and Supplementary Fig. 19);

ii) Their shape, measured as the major and minor axis length of their best fitting ellipsoids (Supplementary Fig. 20 and Supplementary Fig. 21) as well as the aspect ratio between the major and minor axis (Supplementary Fig. 22);

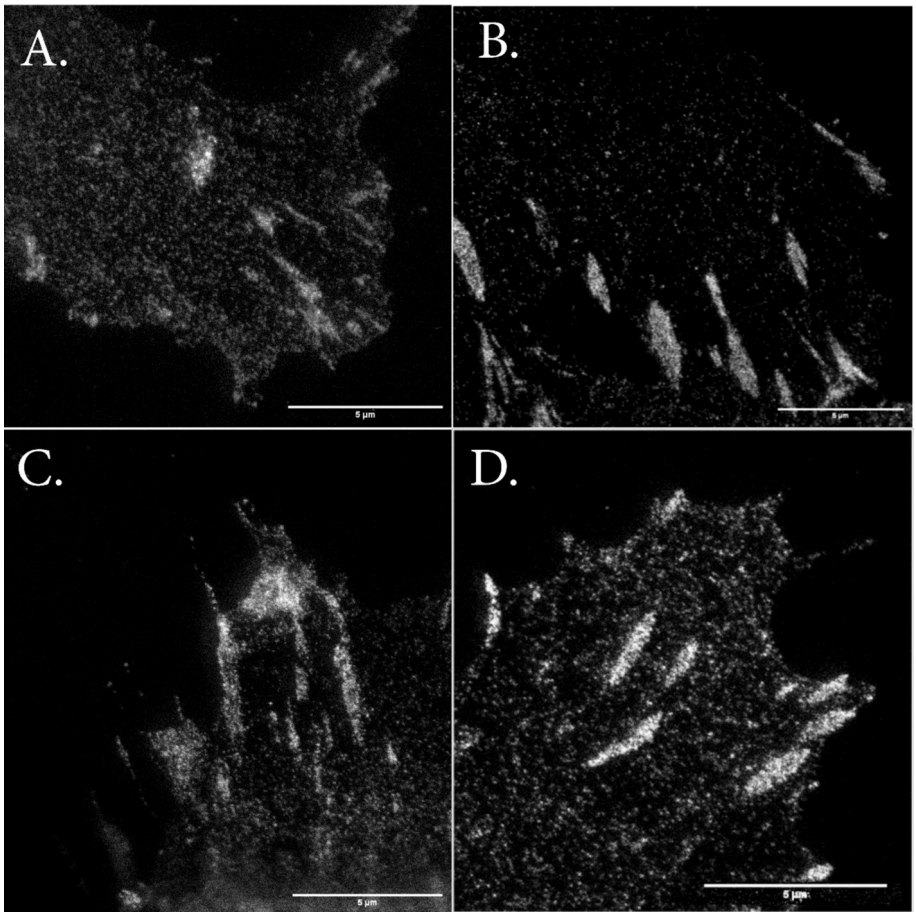

Fig. 7. Representative STED images of the focal adhesions of HDF cells attached onto hemitoroids made by inkjet deposition of different latex blends onto glass: A. 50 % PS, B. 60 % PS, C. 70 % PS, respectively, D. the glass reference substrate. Scale bars of 5 μm marked in each image.

iii) Their roundness (Supplementary Fig. 23).

The morphology of focal adhesion was compared between those of HDF cells grown on a borosilicate glass control (CTRL), and those of HDF cells grown on borosilicate glass substrates with hemitoroidal arrays of three different latex compositions (50 %, 60 %, and 70 % PS) differentiating between focal adhesions attached to glass areas (Glass), the hemitoroid rings (Hemitoroids), and the centre of the hemitoroids (Centre).

Statistically significant differences in focal adhesion area and perimeter length were observed between several surface regions and compositions (Fig. 8, Supplementary Fig. 18, and Supplementary Fig. 19). For the 50 % PS sample, differences in area and perimeter length were observed between the centre of the 50 % PS hemitoroids and the glass control, respectively the hemitoroid region of the 50 % PS sample. In the centre, the focal adhesions were significantly smaller than on other regions elsewhere. Focal adhesion area and perimeter was smaller on the 70 % PS toroids than on the glass reference and on 50 % PS toroids. There were no statistically significant differences between focal adhesions to any region of 60 % PS hemitoroid samples and the other samples in respect to area and perimeter length.

Particularly, the aspect ratio (Supplementary Fig. 22), but also the major axis (Supplementary Fig. 20) showed statistically significant differences for the 50 % PS hemitoroids. The aspect ratio of focal adhesions differed between all regions of the 50 % PS hemitoroid, and also to the glass reference on a at least a 0.9-level. The centre region of the hemitoroids also had a shorter major axis compared to other regions and the control surface. Significant differences in the minor axis were observed for the 50 % PS hemitoroids only between the centre and the hemitoroid region (Supplementary Fig. 21). The 60 % PS hemitoroid sample, on the other hand, showed statistically significant differences in the minor axis, but not the major axis or the aspect ratio. These differences (0.9 level) were observed between all regions of the hemitoroids and, also between the control and the hemitoroid as well as the centre. For 70 % PS hemitoroid samples a statistically significant difference (0.9 level) was only observed between length of the major axis of focal adhesions in the control and the 70 % PS hemitoroids.

In terms of the roundness of the focal adhesions, only the 50 % PS hemitoroids showed statistically significant differences between the different regions of the hemitoroids (Supplementary Fig. 23). Herein, the centre region had the highest roundness, with the hemitoroidal surface causing less round focal adhesions, and the glass regions even less than that. Cells grown on the control surface had a focal adhesion with a similar roundness to those grown on the hemitoroids. There were no observed significant differences between regions in the 60 % PS and 70 % PS hemitoroid samples. Between samples, however, focal adhesions on the 70 % PS hemitoroid had a statistically significantly higher roundness than the 50 % PS and 60 % PS hemitoroids.

4. Discussion

4.1. Observations on the morphology and stiffness of the printed surfaces

Inkjet-printing the latex ink at a relatively low DS onto wetting substrates resulted in even films with a very high optical transparency compared to those produced by drop casting. This was likely a result of the inkjetted films being thinner than the drop-cast films.

On the other hand, printing with a larger DS resulted in a pattern of hemitoroidal structures. That the inkjetted drops takes on a

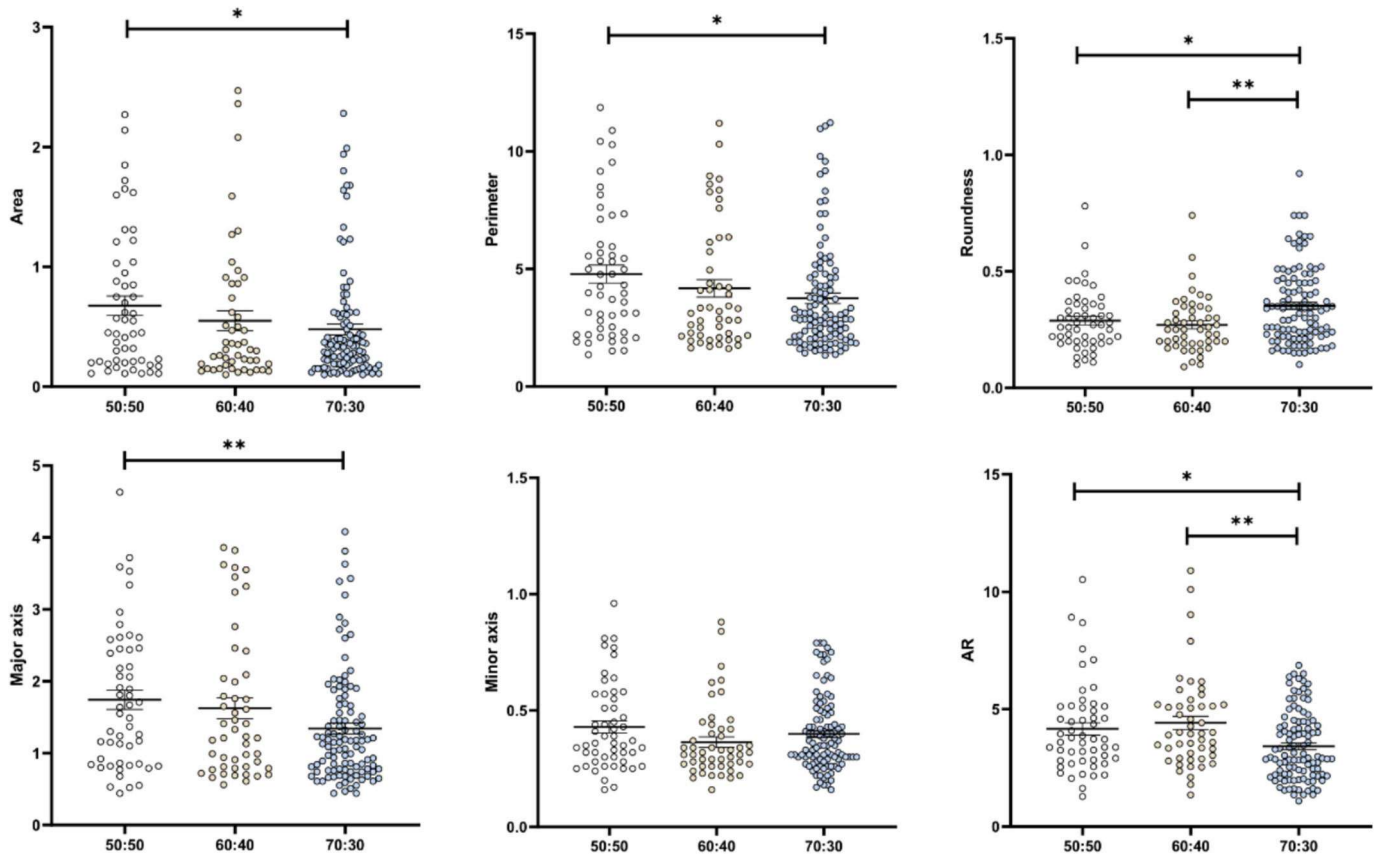

Fig. 8. A comparison of statistical differences between the focal adhesion morphology parameters of HDF cells attached to hemitoroids of different latex composition 50 %PS, 60 % PS, respectively 70 % PS. Top row (left to right) area of focal adhesions [μm^2], perimeter length of focal adhesions [μm], and roundness of focal adhesions [-]; Bottom row (left to right) Major axis length of focal adhesions [μm], minor axis length of focal adhesions [μm], and aspect ratio of focal adhesions (AR) [-]. The values are expressed as means ± SEM, statistical difference was evaluated by the Mann-Whitney test, * $p < 0.05$, ** $p < 0.01$.

hemitoroidal geometry, rather than hemispherical, is likely due to a coffee stain effect. So called 'coffee stains' are formed when the edge of a drop is pinned and the concentration of colloidal particles in the droplets begin to accumulate at said edge [38–40]. As the inkjetted latex dispersion ink droplet dried, this coffee stain effect proposedly caused an accumulation of latex at the droplet periphery resulting in a doughnut-shaped, or hemitoroidal, geometries.

The hemitoroidal surfaces retained a similar nanotopography to that observed for the inkjetted films, both when printed onto glass and onto latex (Figs. 2–3, Supplementary Fig. 1–Supplementary Fig. 5). A nanostructure similar to that which has been seen for drop-cast and rod coated nanostructured latex coatings was also observed for these surfaces, both the films and the hemitoroidal structures [23–28]. The two latex components used in the ink contribute to this structure. The ABS with low T_g is the film forming component which gives integrity to the film. Meanwhile, the PS particles give a nanostructure to the surface with a high T_g, as they retain their spherical shape in the blend, even after IR treatment. However, at the IR treatment stage the PS particles are partially annealed and flattened to give the final structure of the films. The IR treatment has also been observed to disintegrate additives in the film, which can then be removed by washing with MilliQ water [41]. At low PS:ABS ratios, the ABS is likely to cover the whole surface giving a similar surface chemistry between these surfaces [25].

However, the surface structure differed clearly between the central region and the toroidal ring. The central region did not show a nanostructure, but rather a rougher mesh like surface geometry. The differing topography of the centre of the hemitoroids is likely a result of the aforementioned coffee stain effect. As latex dries from the air–liquid interface inward [42], heterogeneous aggregation of latex particles can occur at the droplet surface. In this case, the evaporation of the dispersant mixture, comprising H_2O, EG, and IPA, may have contributed to the formation of the mesh-like pattern through localized particle accumulation and phase separation during solvent loss.

Similarly to previous observations for drop-cast films in [25,26] the amplitude roughness (S_q) of the hemitoroid ring increased with an increasing PS content. Unlike for drop-cast surfaces, however, the S_q increased beyond about 60 % PS, which has seen a smoothening of the film, due to the PS layer being increasingly complete with less and less valleys between particles. The amplitude roughness was on a similar level as that of the drop cast surfaces; S_q was approx. 15 nm for the inkjetted hemitoroid surfaces and approx. 11–13 nm for the surfaces used in [26] and 14 nm in [25]. As said, the surface structure of the 70 % PS hemitoroids was rougher than what has been observed for drop cast films, where 70 % PS surfaces appeared rather flat with occasional valleys [25,26]. This difference suggests that the inkjet printing process, particularly the drying dynamics and particle redistribution, plays a significant role in determining the final surface architecture.

While the topography of the surfaces varied with PS content, no clear difference in the stiffness of 50 % PS, 60 % PS and 70 % PS samples could be observed.

4.2. Cellular responses to the nanostructured surfaces

Cytocompatibility studies of films produced by inkjet printing showed that HDF cell growth is enhanced on latex surfaces compared to said references. This follows the trend of previous results, which show an proliferation enhancing effect of the latex surface [26]. In this case the effect is slight. The likely due to the beneficial surface properties of the

processed film. The topography is likely a main contributor, since the inkjetted latex coating appeared to have a topography that was very similar to what has been observed for the highly beneficial drop-cast latex coatings.

A drawback of these surfaces was their autofluorescence, which slightly reduced the cell imaging quality. For the staining tests the influence was negligible, however, since the stain was chosen so that emission band did not overlap with the autofluorescence region.

4.3. Variations in focal adhesion morphology

4.3.1. Nanotopography-driven differences in focal adhesion morphology

The primary research question that was investigated using the inkjet-printed hemitoroidal arrays was whether variations in nanoscale roughness could drive changes in focal adhesion morphology. To explore this, the focal adhesion descriptors were plotted against the investigated roughness parameters and potential trends were analysed. Since the hemitoroid centres exhibited a similar topography for all inks used regardless of PS:ABS ratio and relatively few focal adhesions were observed per blend in the centre regions, these data points were all combined to one average in the analysis.

A summary of the observed correlations is shown in Table 1. Correlations with a strength above $R^2 > 0.9$ and Pearson's $r \geq |0.95|$ were considered sufficient in this study. These are marked in Table 1 with green. Some examples of the correlation plots are found in Fig. 9. In addition to linear trends, some possible non-linear trends were also noted, for example between S_a respectively S_q and the focal adhesion descriptors aspect ratio and roundness (for example Fig. 9A). Fig. 9 also shows examples of one correlation of adequate quality (Fig. 9B) as well as two disregarded correlation studies (Fig. 9C and D). Corresponding graphs with linear fits are found in the Supporting Information (Supplementary Fig. 24 to Supplementary Fig. 34). Although parameters describing the distribution of heights (S_{sk} and S_{ku}), spacing between asperities (S_{ds} and S_{al}), and peak or valley dominance (S_{sk} and S_{pk}/S_{vk}) were included in the analysis, correlations were primarily observed with amplitude-related parameters (S_a and S_q), the height of the peak and core regions (S_{pk}, S_k) and the functional parameter S_{dr}. Among these, S_{dr} showed the strongest and most consistent correlations, showing correlations with all focal adhesion descriptors except the minor axis.

The influence of the nanostructured topographies on focal adhesion morphology could be summarised as follows; Larger height variations (S_a, S_q) in both the peak area (S_{pk}) reduced the size of the focal adhesions (area and perimeter). An increasing fine structure (S_{dr}, S_k) reduced their elongation (major axis). A fine structure resulted in rounder adhesion structures. Correlations with the S_{dr} and S_k suggest that this may also relate to the abundance of fine structures of the surface to where to the cells can attach with focal adhesions, rather than larger peaks specifically. However, due to the nature of the topographies produced in this study, it was not possible to distinguish the specific effects of sparsely distributed large asperities versus densely packed smaller ones. It is also possible that topographies with larger structures influence the attachment differently. This is hinted at by the plots of focal adhesion aspect ratio and roundness against S_q and S_{dr}, which may indicate diminishing changes in the focal adhesion descriptors at higher roughness levels (Supplementary Fig. 25 and Supplementary Fig. 28). The size of focal adhesions has previously been associated with the substrate stiffness, being shorter on softer substrates compared to stiffer [43]. In this study, no clear differences in substrate stiffness was observed as a result of varying PS content. These surfaces are also rigid, compared to skin, having stiffnesses in the 1.4–2.0 GPa range. Fibroblasts have been observed to respond to stiffnesses up to 20 kPa with changes in their intrinsic stiffness [44], respectively with changes in their alignment over a stiffness gradient up to 120 kPa [45].

Despite these limitations, the observed correlations clearly demonstrate that HDF cell focal adhesions are responsive to nanoscale variations in surface topography. These findings also highlight the importance of using a diverse set of topographical descriptors in cell–surface interaction studies to capture the complexity of biological responses to engineered materials.

5. Conclusions

Inkjet printing proved to be a useful processing method for fabricating nanostructured, two-component latex films. The obtained thin films exhibited a high optical transparency and a tuneable nanotopography. Tuning of surface nanotopography was achieved by adjusting the PS:ABS ratio in the ink. The technique could also be used to make arrays of hemitoroids, with an outer diameter of 30–50 μm and a nanostructured topography, on both borosilicate glass supports and latex-coated microscope glass. The very high (approx. 98 %) optical transparency of the printed latex films minimises the loss in resolution during microscopy using *trans*-illumination, although some autofluorescence is a drawback in fluorescence-based imaging. This can be overcome by choosing staining agents with fluorescence outside this wavelength region (approx. 400–500 nm) [27].

Initially, cytocompatibility tests confirmed that the printed nanostructured films supported HDF cells growth. Later, hemitoroidal arrays were used to study focal adhesion (FA) morphology in HDF cells. The morphology of focal adhesions onto the rings, the centre, and the surrounding glass regions of hemitoroids were compared against the morphology of focal adhesions onto borosilicate glass reference surfaces. The size of focal adhesions, measured as their area and perimeter length, seemed to decrease and their roundness increase with increasing roughness. Even nanoscale differences in roughness parameters provided statistically significant differences in the morphology. For instance, already a change in S_q of 3.9 nm caused differences in area, roundness, and aspect ratio on $p = 0.9$ level and in major axis length at $p = 0.95$. This highlights the utmost sensitivity of cells to nanoscale cues.

Table 1
Correlation matrix of roughness parameters vs. focal adhesion morphology parameters for focal adhesions grown on all surfaces. Apparent correlations with $R^2 > 0.9$ and |Pearson's r| > 0.95 are marked in green.

	Focal adhesion descriptor							
Roughness parameter		**Area**	**Perim.**	**Major**	**Minor**	**Circ.**	**AR**	**Roundn.**
	S_a	$R^2 = 0.894$	$R^2 = 0.906$	$R^2 = 0.857$	$R^2 = 0.246$	$R^2 = 0.872$	$R^2 = 0.536$	$R^2 = 0.699$
		r = -0.946	r = -0.952	r = -0.927	r = -0.496	r = 0.934	r = -0.732	r = 0.836
	S_q	$R^2 = 0.917$	$R^2 = 0.929$	$R^2 = 0.888$	$R^2 = 0.083$	$R^2 = 0.919$	$R^2 = 0.584$	$R^2 = 0.744$
		r = -0.958	r = -0.964	r = -0.942	r = 0.288	r = 0.959	r = -0.764	r = -0.863
	S_{dr}	$R^2 = 0.946$	$R^2 = 0.957$	$R^2 = 0.974$	$R^2 = 0.144$	$R^2 = 0.993$	$R^2 = 0.941$	$R^2 = 0.925$
		r = -0.973	r = -0.978	r = -0.987	r = -0.380	r = 0.996	r = -0.970	r = 0.962
	S_{pk}	$R^2 = 0.953$	$R^2 = 0.956$	$R^2 = 0.878$	$R^2 = 0.251$	$R^2 = 0.824$	$R^2 = 0.450$	$R^2 = 0.453$
		r = -0.976	r = -0.978	r = -0.937	r = -0.501	r = 0.908	r = -0.671	r = 0.673
	S_k	$R^2 = 0.877$	$R^2 = 0.887$	$R^2 = 0.955$	$R^2 = 0.036$	$R^2 = 0.914$	$R^2 = 0.923$	$R^2 = 0.992$
		r = -0.936	r = -0.942	r = -0.977	r = -0.190	r = 0.956	r = -0.961	r = 0.996
	S_{vk}	$R^2 = 0.654$	$R^2 = 0.651$	$R^2 = 0.522$	$R^2 = 0.350$	$R^2 = 0.204$	$R^2 = 0.070$	$R^2 = 0.026$
		r = 0.809	r = 0.807	r = 0.722	r = -0.591	r = -0.452	r = 0.265	r = -0.160

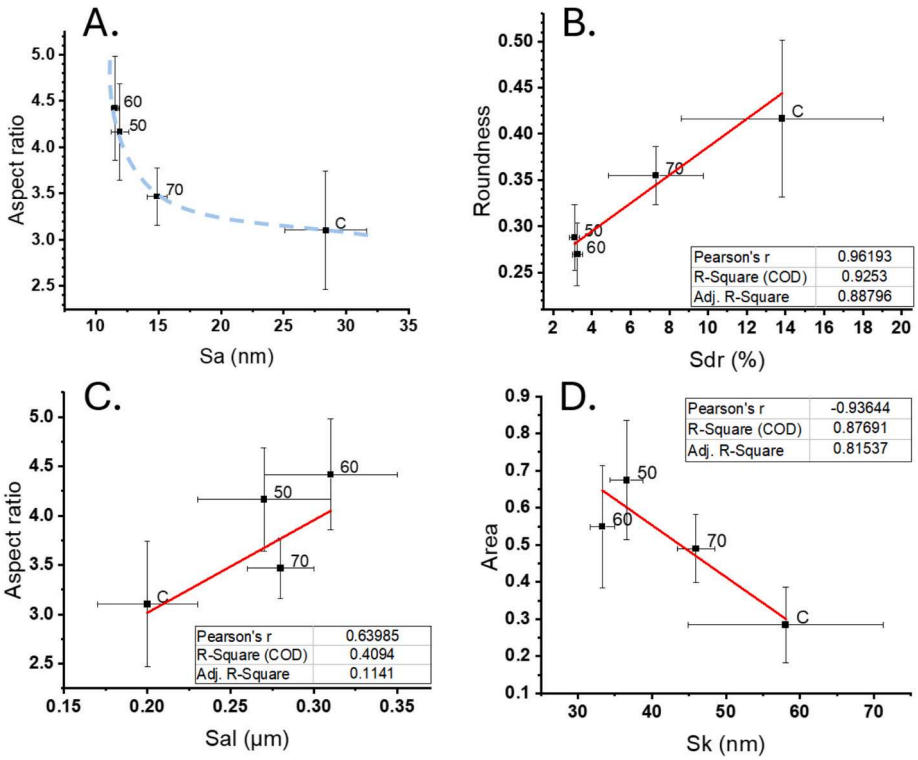

Fig. 9. Examples of the correlation plots: A. The correlation of the aspect ratio of focal adhesions might with the average height variations of the surfaces, might be non-linear. Such correlation was not accounted for in this study. Dashed lines show the authors' interpretation. B. The roundness of the focal adhesions correlated well with the S_{dr} parameter. C. The aspect ratio of the focal adhesions did not correlate with the S_{al} parameter. D. The correlation of the area of the focal adhesions was not strong enough to fulfil the qualification criteria set for the correlation.

These morphological changes correlated strongly ($R^2 \geq 0.9$, Pearson's $r \geq |0.95|$) with roughness parameters describing height variations and fine structure: height variations (S_a, S_q), effective surface area (S_{dr}), peak height above core roughness (S_{pk}), and core roughness (S_k). In contrast, parameters related to feature width and spacing (S_{al}), peak/valley dominance (S_{sk}), density of summits, (S_{ds}) and valley depth (S_{vk}) did not show any clear correlation. This suggests that, for nanometer-scale topographies, cellular responses are primarily driven by height variation rather than lateral spacing or valley depth.

The high processability and scalability of inkjet printing enables these nanostructured coatings to be used on a wide range of surfaces and in an extensive variety of applications. The inherent tunability of polymeric particle dispersions make them particularly interesting in cell-surface interaction studies. With inkjet printing, e.g. material gradient surfaces could easily be produced for studying cellular interactions as a function of material properties. Future work could explore the use of alternative latex formulations and investigate downstream cellular responses, such as signalling pathways and phenotypic changes. It would also be of interest to investigate the variations in the organisation of cytoskeletal elements, as a response to variations in the nanotopography.

This study underscores the importance of nanoscale topography in regulating cellular behaviour and highlights the value of using multiple topographical descriptors in biomaterials research. Such an approach can support both experimental and computational biomaterials design by enabling more precise characterization, comparison, and replication of surface features.

CRediT authorship contribution statement

Emil Rosqvist: Writing – review & editing, Writing – original draft, Visualization, Resources, Methodology, Investigation, Formal analysis, Data curation, Conceptualization. **Anna Fogde:** Writing – review & editing, Methodology, Investigation, Formal analysis, Data curation. **Elnaz Fazeli:** Writing – review & editing, Methodology, Investigation, Formal analysis. **Irina Belaya:** Writing – review & editing, Methodology, Investigation, Formal analysis. **Erik Niemelä:** Writing – review & editing, Methodology, Conceptualization. **Anni Määttänen:** Writing – review & editing, Methodology, Conceptualization. **Arun P. Venu:** . **Pasi Kankaanpää:** Writing – review & editing, Supervision, Methodology, Funding acquisition, Formal analysis. **John E. Eriksson:** Writing – review & editing, Supervision, Methodology, Funding acquisition, Conceptualization. **Jouko Peltonen:** Writing – review & editing, Supervision, Methodology, Funding acquisition, Conceptualization.

Declaration of competing interest

The authors declare that they have no known competing financial interests or personal relationships that could have appeared to influence the work reported in this paper.

Acknowledgements

Rosqvist acknowledges funding from Jane and Aatos Erkko foundation (project: Anti-Bacterial Channelling from Waste to Human Health), Tor, Joe och Pentti Borgs Minnesfond, and Waldemar von Frenckells stiftelse. This research was commenced as part of the Functional Materials at Biological Interfaces Centre of Excellence at Åbo Akademi University.

For service, instrumentation, and expertise we would like to thank the Cell Imaging and Cytometry Core (Turku Bioscience Centre, Turku, Finland) and Turku BioImaging Image Data Team (Turku, Finland), which are part of the Finnish Advanced Microscopy Node of Euro-BioImaging Finland funded by the Research Council of Finland, FIRI grant numbers 328040, 328044.

Parts of the research carried out in this work used Research Council

of Finland Research Infrastructure "Printed Intelligence Infrastructure" (PII-FIRI).

Appendix A. Supplementary data

Supplementary data to this article can be found online at https://doi.org/10.1016/j.matdes.2025.114920.

Data availability

Data will be made available on request.

References

[1] Y. Li, X. Yin, L. Changsheng, The Horizon of Materiobiology: a Perspective on Material-Guided Cell Behaviors and Tissue Engineering, Chem. Rev. 117 (5) (2017) 4376–4421, https://doi.org/10.1021/acs.chemrev.6b00654.

[2] D.-H. Kim, et al., Actin cap associated focal adhesions and their distinct role in cellular mechanosensing, Sci. Rep. 2 (1) (Aug. 2012) 555, https://doi.org/10.1038/srep00555.

[3] M. Rahmati, E. A. Silva, J. E. Reseland, C. A Heyward, and H. J. Haugen, 'Biological responses to physicochemical properties of biomaterial surface.', *Chem. Soc. Rev.*, vol. 49, no. 15, pp. 5178–5224, Aug. 2020, 10.1039/d0cs00103a.

[4] H.M. Rostam, S. Singh, N.E. Vrana, M.R. Alexander, A.M. Ghaemmaghami, Impact of surface chemistry and topography on the function of antigen presenting cells, Biomater. Sci. 3 (3) (2015) 424–441, https://doi.org/10.1039/C4BM00375F.

[5] J.A. Deeg, I. Louban, D. Aydin, C. Selhuber-Unkel, H. Kessler, J.P. Spatz, Impact of local versus Global Ligand Density on Cellular Adhesion, Nano Lett. 11 (4) (Apr. 2011) 1469–1476, https://doi.org/10.1021/nl104079r.

[6] A. Diener, et al., Control of focal adhesion dynamics by material surface characteristics, Biomaterials 26 (4) (2005) 383–392, https://doi.org/10.1016/j.biomaterials.2004.02.038.

[7] M.J. Dalby, M.O. Riehle, H. Johnstone, S. Affrossman, A.S.G. Curtis, In vitro reaction of endothelial cells to polymer demixed nanotopography, Biomaterials 23 (14) (2002) 2945–2954, https://doi.org/10.1016/S0142-9612(01)00424-0.

[8] M.J. Dalby, D. Giannaras, M.O. Riehle, N. Gadegaard, S. Affrossman, A.S.G. Curtis, Rapid fibroblast adhesion to 27nm high polymer demixed nano-topography, Biomaterials 25 (1) (2004) 77–83, https://doi.org/10.1016/S0142-9612(03)00475-7.

[9] T. Sjöström, M.J. Dalby, A. Hart, R. Tare, R.O.C. Oreffo, B. Su, Fabrication of pillar-like titania nanostructures on titanium and their interactions with human skeletal stem cells, Acta Biomater. 5 (5) (2009) 1433–1441, https://doi.org/10.1016/j.actbio.2009.01.007.

[10] J.Y. Lim, et al., The regulation of integrin-mediated osteoblast focal adhesion and focal adhesion kinase expression by nanoscale topography, Biomaterials 28 (10) (2007) 1787–1797, https://doi.org/10.1016/j.biomaterials.2006.12.020.

[11] P. Roca-Cusachs, T. Iskratsch, and M. P. Sheetz, 'Finding the weakest link: exploring integrin-mediated mechanical molecular pathways.', *J. Cell Sci.*, vol. 125, no. Pt 13, pp. 3025–3038, Jul. 2012, 10.1242/jcs.095794.

[12] Y. Wei, Physical Interpretation of the Maximum Receptor−Ligand Bond Spacing to Ensure Cell Adhesion in Ligand-Coated Substrates, Langmuir 24 (11) (Jun. 2008) 5644–5646, https://doi.org/10.1021/la800048e.

[13] A. G. F. de Beer, E. A. Cavalcanti-Adam, G. Majer, M. Lopez-García, H. Kessler, and J. P. Spatz, 'Force-induced destabilization of focal adhesions at defined integrin spacings on nanostructured surfaces.', *Phys. Rev. E Stat. Nonlin. Soft Matter Phys.*, vol. 81, no. 5 Pt 1, p. 051914, May 2010, 10.1103/PhysRevE.81.051914.

[14] H.-C. Lai, L.-F. Zhuang, X. Liu, M. Wieland, Z.-Y. Zhang, Z.-Y. Zhang, The influence of surface energy on early adherent events of osteoblast on titanium substrates, J. Biomed. Mater. Res. A 93A (1) (2010) 289–296, https://doi.org/10.1002/jbm.a.32542.

[15] Y. Hou, et al., Surface Roughness and Substrate Stiffness Synergize to Drive Cellular Mechanoresponse, Nano Lett. 20 (1) (Jan. 2020) 748–757, https://doi.org/10.1021/acs.nanolett.9b04761.

[16] A.N. Generalova, V.P. Zubov, Design of polymer particle dispersions (latexes) in the course of radical heterophase polymerization for biomedical applications, Colloids Surf. B Biointerfaces 166 (Jun. 2018) 303–322, https://doi.org/10.1016/j.colsurfb.2018.03.036.

[17] A. Srivastava, I.B. O'Connor, A. Pandit, J.G. Wall, Polymer-antibody fragment conjugates for biomedical applications, Prog. Polym. Sci. 39 (2) (2014) 308–329, https://doi.org/10.1016/j.progpolymsci.2013.09.003.

[18] S. Fu, J. Lu, X. Luo, F. Bai, Preparation of disperse dye/latex dispersion for printing of cellulose fabric, Colloids Surf. Physicochem. Eng. Asp. 423 (2013) 131–138, https://doi.org/10.1016/j.colsurfa.2013.01.037.

[19] D. Bandera, V. R. Meyer, D. Prevost, T. Zimmermann, and L. F. Boesel, 'Polylactide/Montmorillonite Hybrid Latex as a Barrier Coating for Paper Applications.', *Polymers*, vol. 8, no. 3, Mar. 2016, 10.3390/polym8030075.

[20] G. Mauthner, et al., Inkjet printed surface cell light-emitting devices from a water-based polymer dispersion, Org. Electron. 9 (2) (2008) 164–170, https://doi.org/10.1016/j.orgel.2007.10.007.

[21] Y. Yang, M. Li, S. Fu, Screen-printed photochromic textiles with high fastness prepared by self-adhesive polymer latex particles, Prog. Org. Coat. 158 (2021) 106348, https://doi.org/10.1016/j.porgcoat.2021.106348.

[22] B.B. Mesic, L. Järnström, J. Johnston, Latex-based barrier dispersion coating on linerboard: Flexographic multilayering versus single step conventional coating technology, Nord. Pulp Pap. Res. J. 30 (2) (2015) 350–360, https://doi.org/10.3183/npprj-2015-30-02-p350-360.

[23] E. Rosqvist, et al., Low-cost, mass-producible nanostructured surface on flexible substrate with ultra-thin gold or silver film for SERS applications, Nano-Struct. Nano-Objects 34 (2023) 100956, https://doi.org/10.1016/j.nanoso.2023.100956.

[24] U. Gradišar Centa, M. Sterniša, B. Višić, Ž. Federl, S.S. Možina, M. Remškar, Novel nanostructured and antimicrobial PVDF-HFP/PVP/MoO3 composite, Surf. Innov. 9 (5) (2021) 256–266, https://doi.org/10.1680/jsuin.20.00073.

[25] P. San-Martin-Galindo, et al., Modulation of virulence factors of Staphylococcus aureus by nanostructured surfaces, Mater. Des. 208 (Oct. 2021) 109879, https://doi.org/10.1016/j.matdes.2021.109879.

[26] E. Rosqvist, et al., Human dermal fibroblast proliferation controlled by surface roughness of two-component nanostructured latex polymer coatings, Colloids Surf. B Biointerfaces 174 (2019) 136–144, https://doi.org/10.1016/j.colsurfb.2018.10.064.

[27] E. Rosqvist, E. Niemelä, S. Liang, J. E. Eriksson, X. Wang, and J. Peltonen, 'Proliferation of Human Cervical Cancer Cells Responds to Surface Properties of Bicomponent Polymer Coatings.', *Nanomater. Basel Switz.*, vol. 15, no. 10, May 2025, 10.3390/nano15100716.

[28] E. Rosqvist, et al., A low-cost paper-based platform for fast and reliable screening of cellular interactions with materials, J. Mater. Chem. B 8 (6) (2020) 1146–1156, https://doi.org/10.1039/C9TB01958H.

[29] A. Määttänen, A. Fallarero, J. Kujala, P. Ihalainen, P. Vuorela, J. Peltonen, Printed paper-based arrays as substrates for biofilm formation, AMB Express 4 (1) (Jun. 2014) 32, https://doi.org/10.1186/s13568-014-0032-0.

[30] A. Määttänen, P. Ihalainen, B. Törngren, E. Rosqvist, M. Pesonen, J. Peltonen, Hierarchically structured self-supported latex films for flexible and semi-transparent electronics, Appl. Surf. Sci. 364 (2016) 37–44, https://doi.org/10.1016/j.apsusc.2015.12.088.

[31] B. Bhushan, 'Surface roughness analysis and measurement techniques', 2000, pp. 49–119.

[32] D. Whitehouse, '3 - Profile and areal (3D) parameter characterization', in *Surfaces and Their Measurement*, D. Whitehouse, Ed., Oxford: Kogan Page Science, 2002, pp. 48–95. [Online]. Available: http://www.sciencedirect.com/science/article/pii/B9781903996010500037.

[33] R.J. Crawford, H.K. Webb, V.K. Truong, J. Hasan, E.P. Ivanova, Surface topographical factors influencing bacterial attachment, Adv. Colloid Interface Sci. 179–182 (2012) 142–149, https://doi.org/10.1016/j.cis.2012.06.015.

[34] K.N. Hansson, S. Hansson, Skewness and Kurtosis: Important Parameters in the Characterization of Dental Implant Surface Roughness—A Computer simulation, ISRN Mater. Sci. 2011 (Oct. 2011) 305312, https://doi.org/10.5402/2011/305312.

[35] J. Järnström, P. Ihalainen, K. Backfolk, J. Peltonen, Roughness of pigment coatings and its influence on gloss, Appl. Surf. Sci. 254 (18) (2008) 5741–5749, https://doi.org/10.1016/j.apsusc.2008.03.043.

[36] D.J. Whitehouse, *Handbook of Surface and Nanometrology*, 2nd ed., CRC Press, Boca Raton, Florida, US, 2010.

[37] J. Schindelin, C.T. Rueden, M.C. Hiner, K.W. Eliceiri, The ImageJ ecosystem: an open platform for biomedical image analysis, Mol. Reprod. Dev 82 (7–8) (2015) 518–529, https://doi.org/10.1002/mrd.22489.

[38] M.J. Hertaeg, C. Rees-Zimmerman, R.F. Tabor, A.F. Routh, G. Garnier, Predicting coffee ring formation upon drying in droplets of particle suspensions, J. Colloid Interface Sci. 591 (2021) 52–57, https://doi.org/10.1016/j.jcis.2021.01.092.

[39] R.D. Deegan, O. Bakajin, T.F. Dupont, G. Huber, S.R. Nagel, T.A. Witten, Capillary flow as the cause of ring stains from dried liquid drops, Nature 389 (6653) (Oct. 1997) 827–829, https://doi.org/10.1038/39827.

[40] R.D. Deegan, O. Bakajin, T.F. Dupont, G. Huber, S.R. Nagel, T.A. Witten, Contact line deposits in an evaporating drop, Phys. Rev. E 62 (1) (Jul. 2000) 756–765, https://doi.org/10.1103/PhysRevE.62.756.

[41] H. Juvonen, A. Määttänen, P. Ihalainen, T. Viitala, J. Sarfraz, J. Peltonen, Enhanced protein adsorption and patterning on nanostructured latex-coated paper, Colloids Surf. B Biointerfaces 118 (2014) 261–269, https://doi.org/10.1016/j.colsurfb.2014.03.050.

[42] P.A. Steward, J. Hearn, M.C. Wilkinson, An overview of polymer latex film formation and properties, Adv. Colloid Interface Sci. 86 (3) (2000) 195–267, https://doi.org/10.1016/S0001-8686(99)00037-8.

[43] S. J. Han, K. S. Bielawski, L. H. Ting, M. L. Rodriguez, and N. J. Sniadecki, 'Decoupling substrate stiffness, spread area, and micropost density: a close spatial relationship between traction forces and focal adhesions.', *Biophys. J.*, vol. 103, no. 4, pp. 640–648, Aug. 2012, 10.1016/j.bpj.2012.07.023.

[44] J. Solon, I. Levental, K. Sengupta, P. C. Georges, and P. A. Janmey, 'Fibroblast adaptation and stiffness matching to soft elastic substrates.', *Biophys. J.*, vol. 93, no. 12, pp. 4453–4461, Dec. 2007, 10.1529/biophysj.106.101386.

[45] F. Zhao, et al., Fibroblast alignment and matrix remodeling induced by a stiffness gradient in a skin-derived extracellular matrix hydrogel, Acta Biomater. 182 (2024) 67–80, https://doi.org/10.1016/j.actbio.2024.05.018.